






Influence of particle size on powder velocity distribution at the nozzle outlet in Directed Energy Deposition

Tijan Mede^{a, , *}, Andrej Jeromen^{b, ,} Edvard Govekar^{b, ,} Michael Mallon^{c, ,}
Matjaž Godec^{a, }

^a Institute of Metals and Technology, Lepi pot 11, Ljubljana, 1000, Slovenia

^b Faculty of Mechanical Engineering, Aškerčeva cesta 6, Ljubljana, 1000, Slovenia

^c European Space Research and Technology Centre, European Space Agency, Keplerlaan 1, Noordwijk, 2201 AZ, Netherlands

ARTICLE INFO

Keywords:

Directed Energy Deposition
Powder stream
Boundary conditions
Particle velocity distribution

ABSTRACT

Metal-based Directed Energy Deposition (DED) is considered one of the variations of additive manufacturing with the highest potential, particularly for space industry and in-orbital manufacturing. The technology however still faces various challenges, many of which can be traced back to poor control and understanding of the powder delivery. Velocity distribution of powder particles at the DED nozzle outlet has a key influence on the results of any predictive model of powder stream and yet remains largely disputed. Certain numerical studies highlighted a possible influence of powder particle size on the velocity condition at the nozzle exit, yet no experimental studies confirmed this effect. The experimental campaign described in this paper quantifies this relation between powder particle size and velocity distribution at the nozzle outlet and a strong decrease of particle speed with particle size is observed. Moreover, smaller particles are observed to travel at speeds higher than the mean carrier gas speed suggesting powder particle segregation within the nozzle as one of the mechanisms driving speed differences at the nozzle outlet.

1. Introduction

Additive manufacturing (AM) is regularly referred to as a disruptive technology due to the wide range of new possibilities it is opening up across a variety of different fields [1]. The demand for high-performance and low-weight structures make this technology particularly interesting for the aerospace sector [2]. Directed Energy Deposition (DED) above all the other variations of AM is considered to have the most significant potential for space industry and in-orbital manufacturing due to no imposed limitation on the size of the manufactured objects and its ability to operate in microgravity [3,4].

The state of DED technology however doesn't yet match the high performance objectives dictated by the space industry. Among the more acute drawbacks of DED are the relatively poor dimensional accuracy, lack of fusion and other recurring structural defects. While the end result of DED process is a complex interplay of various factors, it is generally agreed that the inherently stochastic nature of the powder stream lies at the heart of these drawbacks [5–7]. Increased accuracy of the blown

powder dynamics is therefore considered a crucial ingredient of next-generation DED simulation models [8].

A variety of different approaches has been employed in the past two decades to simulate the powder stream in DED. Analytical approaches typically assume an idealized Gaussian distribution of powder particles along the powder stream and compute particle trajectories by extrapolation of the nozzle passages [7,9,10]. Numerical approaches on the other hand usually rely on computational fluid dynamics (CFD) to resolve a two-phase flow problem involving a dispersed second phase with the additional transport equation for the powder phase [11–14]. In either case the powder stream behaviour is largely governed by the velocity distribution of powder particles exiting the nozzle, making the powder velocity boundary condition a crucial point of any model.

Early modelling approaches assume a uniform powder speed at the nozzle outlet that matches that of the carrier gas and particle divergence angles that vary within the range of estimated values [15–17]. Some of the more recent numerical approaches extended the simulated domain to include a certain length of the DED nozzle inner walls upstream of the

* Corresponding author.

E-mail address: tijan.mede@imt.si (T. Mede).

<https://doi.org/10.1016/j.matdes.2025.114680>

Received 23 January 2025; Received in revised form 22 July 2025; Accepted 31 August 2025

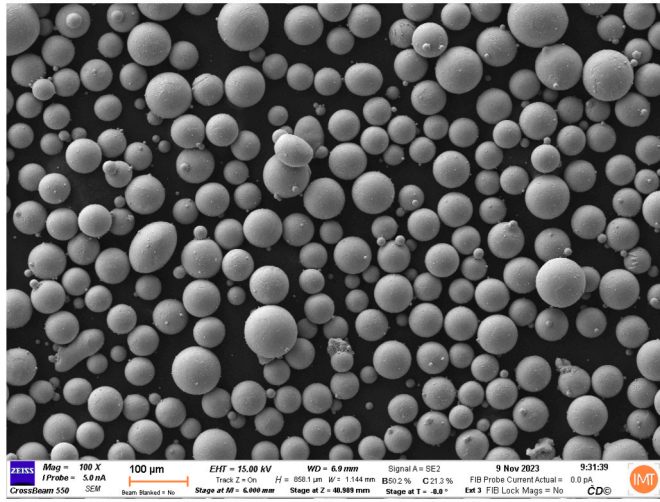


Fig. 1. SEM image of the AP&C Spherical APA Ti-6Al-4V powder prior to sieving.

outlet [13,18,6,19] and thus attempted to avoid the need for experimental evaluation of the powder boundary conditions. A boundary condition further upstream nevertheless needed to have been assumed and similarly as in previous approaches a uniform powder velocity matching that of the carrier gas was applied. CFD-based numerical results of these studies indicated that the powder speed at the nozzle outlet diminishes with the powder particle size on the account of the loss of momentum of the larger powder particles through the plastic collisions with the inner nozzle walls, while the smaller particles with sufficiently low Stokes numbers follow the carrier gas streamlines and avoid the loss of momentum through particle-wall collisions. The simulated dynamics of these studies however depend heavily on the law of particle interaction with the nozzle walls [6] which had to be assumed. This effect of the powder particle size on the powder velocity distribution at the nozzle outlet has also never been experimentally validated and remains a numerically elaborated concept. Concurrently various other models assume the powder velocity to be independent of the particle size [20,7].

An original approach is thus developed and utilised to measure the powder particle velocity at the nozzle outlet of a commercially available DED deposition head and analyse the powder velocity dependence on the powder particle size.

2. Experiment

2.1. Powder preparation & analysis

AP&C Spherical APA Ti-6Al-4V powder (Fig. 1) was used for this experiment. Prior to experimental runs the powder was analysed and treated as described in the following paragraphs.

Sphericity of the utilized powder particles was first analysed using an Xradia microXCT-400 high resolution 3D X-ray imaging system with a resolution of 2 µm. A sample of 2460 powder particles was scanned for the analysis. Applying a proprietary segmentation algorithm, individual powder particles were identified and used to calculate particle sphericity values. Distribution of particle sphericities can be observed in Fig. 2, while mean sphericity was evaluated at $\bar{\phi} = 0.88$ and median sphericity was evaluated at $\phi^m = 0.89$.

The Ti-6Al-4V powder was then separated into different size fractions using sieving. The sieving was performed using the HAVER EML 315 digital plus test sieve shaker and a set of HAVER & BOECKER Nexpart $\phi 250$ mm x 55 mm stainless steel mesh sieves (45 µm, 63 µm, 75 µm, 100 µm, 125 µm, 150 µm, 200 µm). In order to verify that the powder separation procedure was successful, samples of several hundred particles were taken from each size fraction and analysed under a Thermo Fischer Scientific Apreo 2 SEM microscope. Distributions of

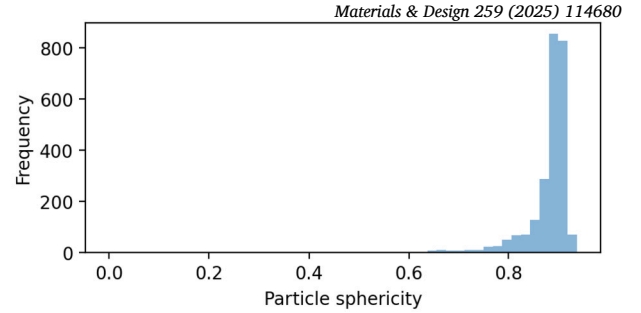


Fig. 2. A histogram of the particle sphericities for the analysed sample of AP&C Spherical APA Ti-6Al-4V particles.

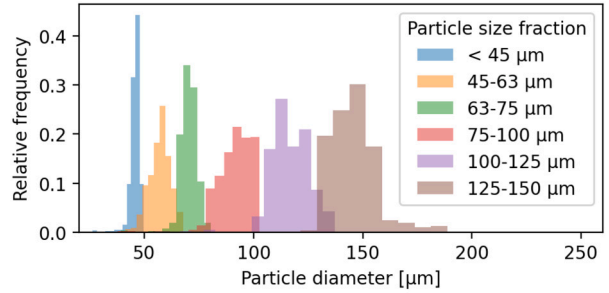


Fig. 3. Histograms of powder particle size distributions for individual size fractions after the digital analysis of SEM images. Contributions of individual particles to the size distributions are weighted by the particle volumes to filter out the contribution of extremely small particles.

Table 1

Table with mean powder particle diameters \bar{d}_{eq} and shares of total volume of powder particles within the fraction bounds $V_{\%}$ for each powder size fraction (marked by the lower bound L and upper bound U) respectively.

Size fraction	\bar{d}_{eq}	$V_{\%}$
< 45 µm	45.48 µm	0.99
45-63 µm	56.83 µm	0.99
63-75 µm	69.98 µm	0.99
75-100 µm	91.12 µm	0.99
100-125 µm	116.31 µm	0.99
125-150 µm	144.91 µm	0.95

equivalent powder particle radii d_{eq} were obtained from the digital SEM images, assuming perfect particle sphericity. In order to filter out the contributions of the extremely small powder particles and numerical artefacts of image processing (which are numerous in terms of quantity but negligible in terms of volume), the contributions of individual particles to the distributions were weighted by particle volumes (assuming perfect particle sphericity). Histograms of weighted equivalent particle radii distributions are shown in Fig. 3.

Table 1 summarizes the results of the powder separation procedure analysis. The column \bar{d}_{eq} lists the mean equivalent particle diameter (henceforth also referred to as the mean particle size) for each individual powder size fraction. The column $V_{\%}$ lists the share of total volume of powder particles within the bounds $\pm 10\%$ of that fraction for each size fraction:

$$V_{\%} = \frac{\sum \frac{4\pi(0.5*d)^3}{3} \text{ if } (0.9 \cdot L \leq d \leq 1.1 \cdot U)}{\sum \frac{4\pi(0.5*d)^3}{3}}, \quad (1)$$

where d is the equivalent diameter of the individual powder particles, L is the lower bound of the individual size fraction and U is the upper bound of the individual size fraction.

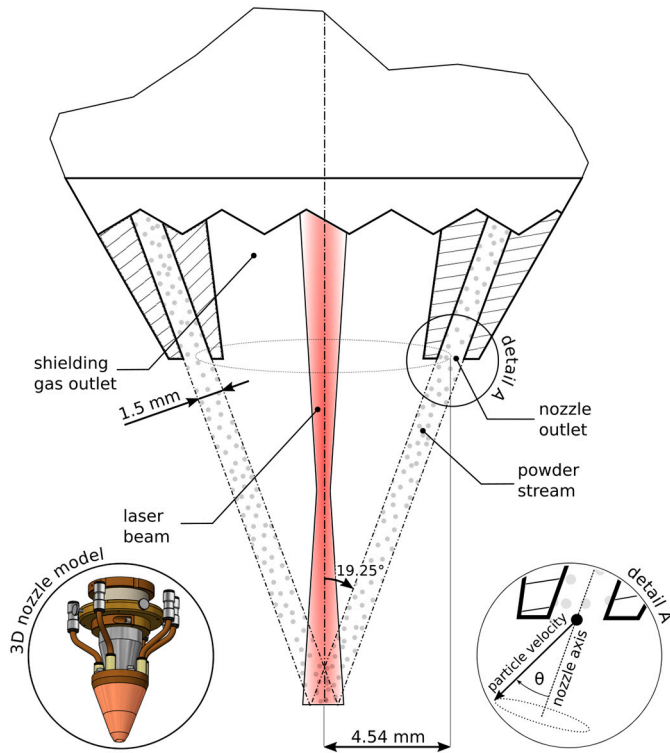


Fig. 4. Fraunhofer COAX 12V5 discrete coaxial deposition head used for the powder particle velocity measurements at the nozzle outlets. Only two nozzle outlets (of the total four) can be observed in this cross-section. For more details on the deposition head geometry refer to Appendix A.

2.2. Powder velocity measurements

The powder velocity measurements were performed on a commercially available Fraunhofer COAX 12V5 discrete coaxial deposition head with four nozzles. Construction details of the deposition head are supplied in Fig. 4 and Appendix A. A constant volumetric flow rate $Q_g = 5$ L/min of the Argon carrier gas was used for all the measurements. The powder was supplied by a GTV PF 2/2 powder feeder at a constant rate of 0.5 rpm of the feed disc, resulting in a powder mass flow rate of $\dot{m} = 1.7$ g/min. No shielding gas was applied during the execution of the experiments and the laser beam was switched off.

The velocity of the particles below the DED deposition head was measured optically. For this purpose, powder streams from the two opposing nozzles were illuminated with a laser light plane (Fig. 5) generated by a line laser (Coherent StingRay-660) with a power of 50 mW and a wavelength of 660 nm. The vertical laser light plane with a thickness of approximately 0.3 mm was aligned with the axis of the two nozzle outlets and with the axis of the DED deposition head (Fig. 5). The output power of the line laser was modulated with a 30 kHz square wave signal between 0% and 100%. Images of the illuminated particles were captured by a monochrome digital camera (Point Grey GS3-U3-23S6M) positioned perpendicular to the laser light plane (Fig. 5). The camera was equipped with a 75 mm focal length lens (Navitar MVL75M1) and a 45 mm extension ring containing a bandpass filter with a central wavelength of 650 nm and a half maximum width of 40 nm to minimize the influence of ambient illumination. The images were captured at 80 frames per second, a resolution of 1920×1200 pixels with 8 bits and an exposure time of 0.2 ms. The size of the square image pixels corresponded to a length of $9.03 \mu\text{m}$. In order to obtain a sufficiently large sample of particle traces, 50,000 images were taken for each individual powder size fraction.

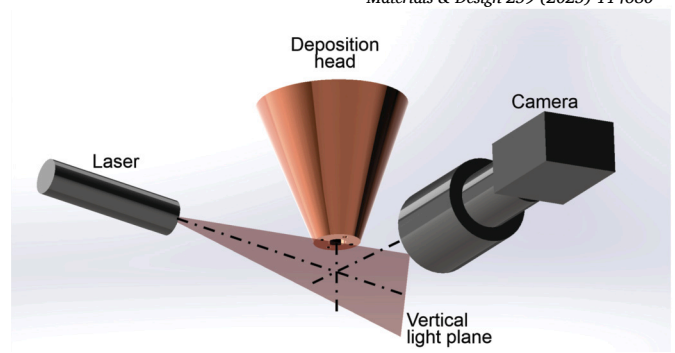


Fig. 5. Schematic representation of the experimental setup.

2.3. Post-processing

Sets of images that were obtained for each individual powder size fraction measurement were post-processed with a Python-based script that was developed in the scope of this project to extract powder particle velocities (Fig. 6). A sensitivity analysis of the key measured variables to the parameters of image processing is described in Appendix B. Grayscale images obtained during the experimental runs feature dashed traces of passing particles that result from the particles reflecting the modulated laser source illumination. After thresholding the grayscale images (sensitivity analysis in Fig. 16), Hough transformation is applied in order to identify straight lines. The Hough transformation results in a multitude of line candidates for each particle trace as the thresholded traces have a width of several pixels. The line candidates representing the same particle trace are identified by performing hierarchical clustering in the space consisting of the upper and lower coordinates of the line candidates (sensitivity analysis in Fig. 17). A single trace line representative of the corresponding particle path is identified in each line cluster by calculating the medians of the two end points of all the line candidates in the corresponding cluster.

Once the particle traces are identified, their speed is evaluated. The commonly adopted approach of evaluating the particle speed from the length of the trace [5,21,13] is susceptible to errors due to particles moving into- or out- of- the illuminated domain during the camera acquisition time and consequently resulting in a shorter illuminated trace on the recorded image. In order to avoid this error, particle speed is evaluated from the period length and the frequency of the laser light source modulation. The period length is computed from the auto-correlation function of the binary image value along the identified trace line.

In order to assure the analysis result reflects the powder boundary conditions at the DED nozzle outlets, only a subset of powder particle traces sufficiently close to the nozzle outlet were considered for the velocity estimation. Only particle traces with the vertical coordinate of the central point $y_c < y_{max} = 2$ mm were filtered out for the powder particle velocity analysis (sensitivity analysis in Fig. 18).

3. Results & analysis

This section summarizes the results of the measurements of powder particle velocity by analysing particle speed v and particle divergence angle θ (see Fig. 4, detail A). Approximating functions are fitted over the measured data in an attempt to model the observed influence of particle size on the powder velocity.

3.1. Powder particle speed

Measured particle speed distributions at the DED nozzle outlet are displayed in Fig. 7. Curves in the plot represent Gaussian kernel density estimations (KDE) of the measured speed distributions for each respective powder particle size fraction applying Scott's Rule bandwidth estimation. The speed distributions appear Gaussian-like and exhibit a

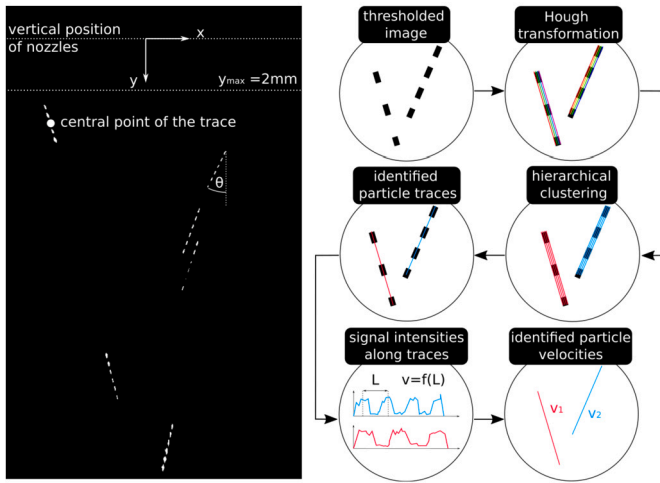


Fig. 6. The left side of the image shows an example of the obtained image from the high-speed camera. The added annotations mark the coordinate axes, divergence angle θ , the central point of a trace and the vertical limit of the domain, where the boundary conditions were measured y_{max} . The right side of the image depicts a schematic process chart of the image post-processing procedure.

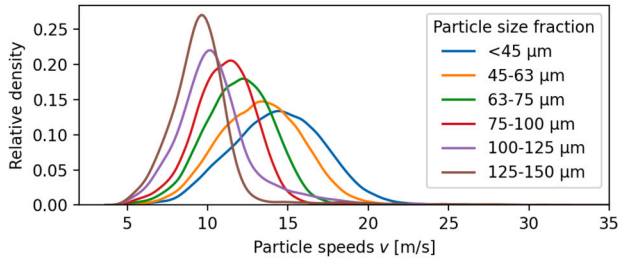


Fig. 7. KDEs of measured particle speed distributions for individual powder particle size fractions.

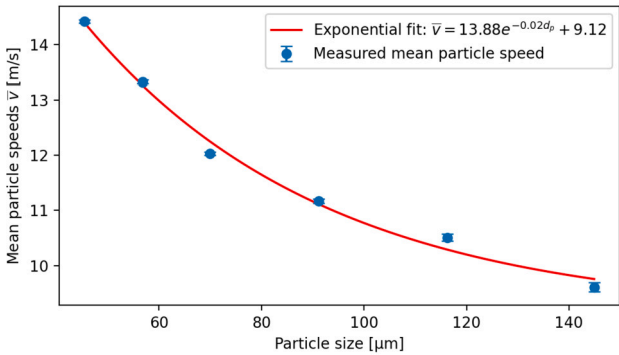


Fig. 8. Measured values of mean particle speed \bar{v} as a function of particle size d_p with 95% confidence intervals (in blue) and a fitted exponential function (in red).

strong dependence on the powder particle size, which is further detailed in the following paragraphs.

Mean powder particle speeds \bar{v} with 95% confidence intervals for each individual powder size fraction are plotted against the mean particle size within corresponding powder size fractions in Fig. 8. The mean particle speeds exhibit a quasi exponential decrease with the mean particle size. As an approximative model, an exponential function was fitted to the speed measurements data and the quality of the fit was evaluated by computing the coefficient of determination $R^2(\bar{v}) = 0.99$. The function and the values of its parameters are included in Fig. 8.

The standard deviations σ_v of measured particle speeds with 95% confidence intervals for each individual powder size fraction are plot-

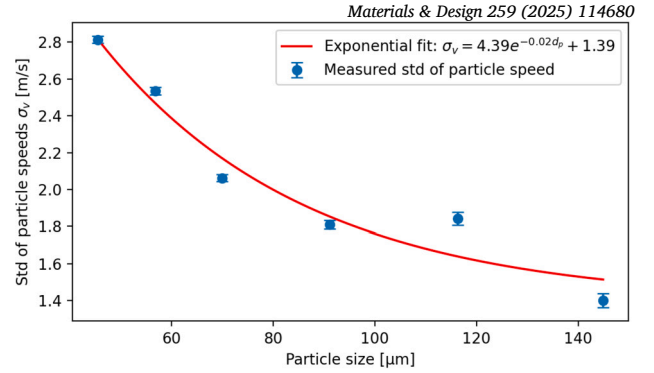


Fig. 9. Measured standard deviations of particle speed σ_v as a function of particle size d_p with 95% confidence intervals (in blue) and a fitted exponential function (in red).

ted against the mean particle sizes within corresponding powder size fractions in Fig. 9. Interquartile Range (IQR) method was used to remove speed outliers from the measured dataset for the calculation of σ_v . Outliers are defined as the speed measurement instances that fall outside of the range, defined as 1.5 times the IQR above the upper quartile (Q3) and below the lower quartile (Q1). The dataset exhibits a rapid, non-linear decrease of σ_v with the mean particle size. An exponential function was fitted over the measured data to approximate the speed standard deviation dependency on powder particle size. The coefficient of determination for the fitted exponential function is $R^2(\sigma_v) = 0.95$. The function and the values of its parameters are included in Fig. 9.

The fitted models for \bar{v} and σ_v can now be used to generate idealized Gaussian distributions of powder particle speed at the nozzle outlet and evaluate the quality of fit with the actual measured particle speed distributions. Fig. 10 displays the modelled speed distributions and KDEs of measured particle speed distributions as well as corresponding coefficients of determination that evaluate the quality of fit for each individual powder particle size fraction.

3.2. Powder particle divergence angle

Interquartile Range (IQR) method was used to remove θ outliers from the measured dataset before analysing the powder particle divergence angles. Outliers were defined as the θ measurement instances that fall outside of the range, defined as 1.5 times the IQR above the upper quartile (Q3) and below the lower quartile (Q1).

The distributions of powder particle divergence angles θ at the DED nozzle outlet for each respective powder size fraction are presented in Fig. 11 as a function of mean particle size. Curves in the plot represent Gaussian kernel density estimations of the measured divergence angles applying Scott's Rule bandwidth estimation. Divergence angle distributions exhibit Gaussian-like shape. Mean values and standard deviations of divergence angles are analysed in the following paragraphs.

Mean values of the powder particle divergence angles $\bar{\theta}$ with 95% confidence intervals for each individual powder size fraction are plotted against mean particle sizes of corresponding powder size fractions in Fig. 12. $\bar{\theta}$ values display minimal variation around the zero angle. A zero-value constant function is thus considered sufficient to approximate the dependence of $\bar{\theta}$ on powder particle size as shown in Fig. 12.

The standard deviations of the powder particle divergence angles σ_θ with 95% confidence intervals for each individual powder size fraction are plotted against mean particle sizes of corresponding powder size fractions in Fig. 13. The measured instances of σ_θ are dispersed around the value 4° and a relatively weak negative correlation between the divergence angle and particle size is observed. As an approximative model, a linear function was fitted to the σ_θ measurements and the quality of the fit was evaluated by computing the coefficient of determination $R^2(\sigma_\theta) = 0.58$. The fitted function and the values of its parameters are included in Fig. 13.

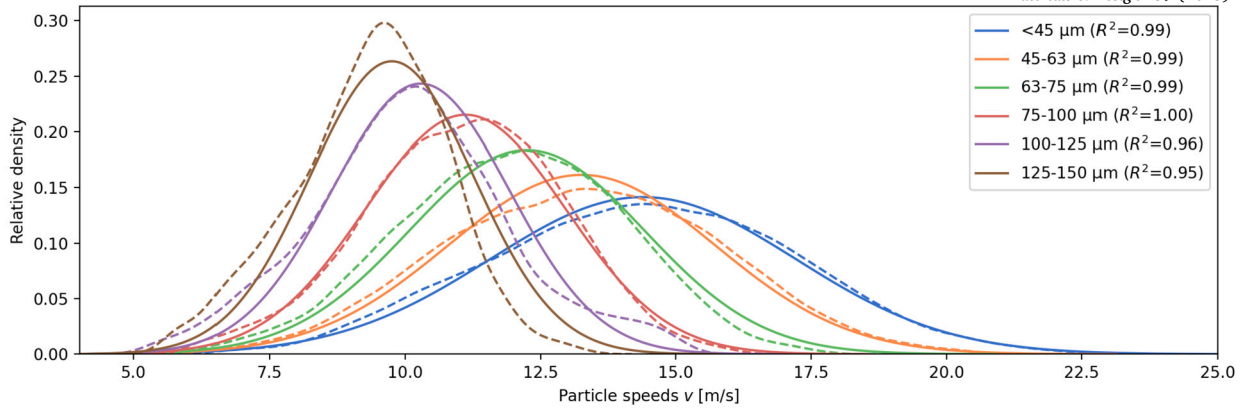


Fig. 10. The modelled particle speed distributions (in solid lines) and KDEs of measured particle speed distributions (in dashed lines) for individual powder particle size fractions. Values of coefficients of determination R^2 measuring the quality of the fit between the modelled and measured speed distribution for each particle size fraction are also displayed.

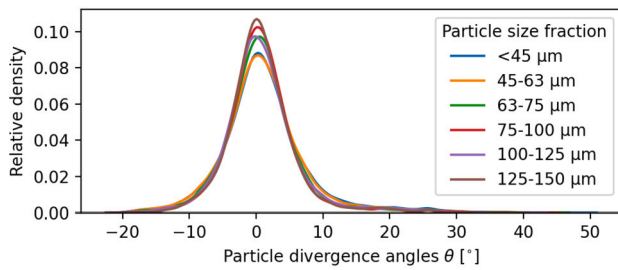


Fig. 11. KDEs of measured particle divergence angle θ distributions for individual powder particle size fractions.

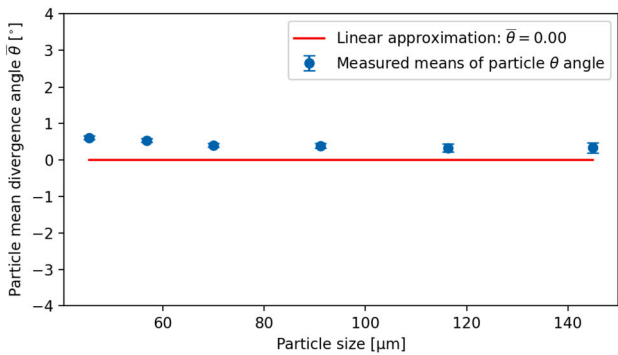


Fig. 12. Measured mean values of particle divergence angle as a function of particle size with 95% confidence intervals (in blue) and an approximating linear function (in red).

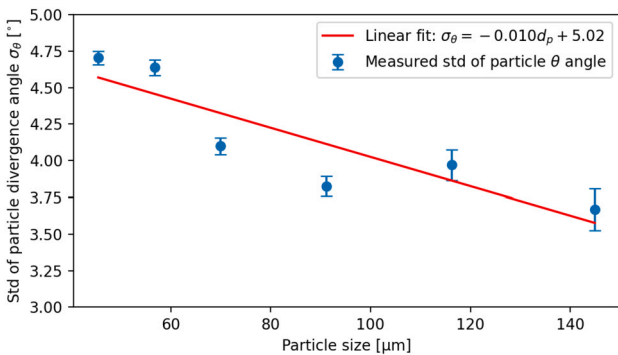


Fig. 13. Measured standard deviations of particle divergence angle as a function of particle size with 95% confidence intervals (in blue) and a fitted linear function (in red).

The fitted models for $\bar{\theta}$ and σ_{θ} are used to generate idealized Gaussian distributions of powder particle divergence angles at the DED nozzle outlet and evaluate the quality of fit with the measured particle divergence angle distributions. Fig. 14 exhibits the modelled divergence angle distributions and KDEs of measured particle divergence angle distributions as well as corresponding coefficients of determination that quantify the quality of fit for each individual powder particle size fraction.

4. Discussion

The utilized Ti-6Al-4V powder was shown to be highly spherical with the mean and median particle sphericity close to 0.9 (Fig. 2). X-ray tomography 3D images as well as SEM microscopy images of the powder exhibit well-rounded particles with occasional instances of smaller satellite particles attached to the surface of larger particles and rare instances of elongated particles. The powder sieving procedure was shown to produce a good segregation of powder particle size distributions with well separated values of corresponding mean particle sizes (Table 1). The particle size distributions of individual size fractions exhibit some overlap at the edges of distributions (Fig. 3). On one hand, the existence of a smaller fraction of powder particles below the lower threshold of respective powder size fractions could be attributed to imperfect sieving, where not all of the powder particles small enough to fit through a sieve were forced through it. On the other hand, the existence of a smaller fraction of powder particles above the upper threshold of respective powder size fractions could be attributed to elongated particles, which can, if correctly oriented, pass through sieve apertures smaller than their equivalent spherical diameter. Nevertheless, the powder sieving produced good results that allowed powder particle velocity distributions to be analysed against mean particle sizes of individual fractions. While the minor overlap of particle size fractions could be expected to have an effect on the spread of measured powder particle velocities, the magnitude of that effect is considered marginal.

The powder particle velocity measurements presented in this paper are performed by analysing planar images of particle reflections during the camera acquisition time, necessarily introducing an error due to non-zero powder particle velocity perpendicular to the image plane. This is an established approach to measuring powder particle velocities in DED powder stream [13,22,18,23,24] and it is generally assumed that the error due to out-of-plane particle velocities is sufficiently small to be neglected. Smurov et al. [22] estimated this error in a conical-like particle flux with 18° angle relatively to the substrate to about 5%. As no variation in the particle divergence angle was taken into account, this error should be considered the upper limit for the out-of-plane velocity error - at this particular divergence angle of the powder stream. In the present study this error was measured using a secondary high-speed camera,

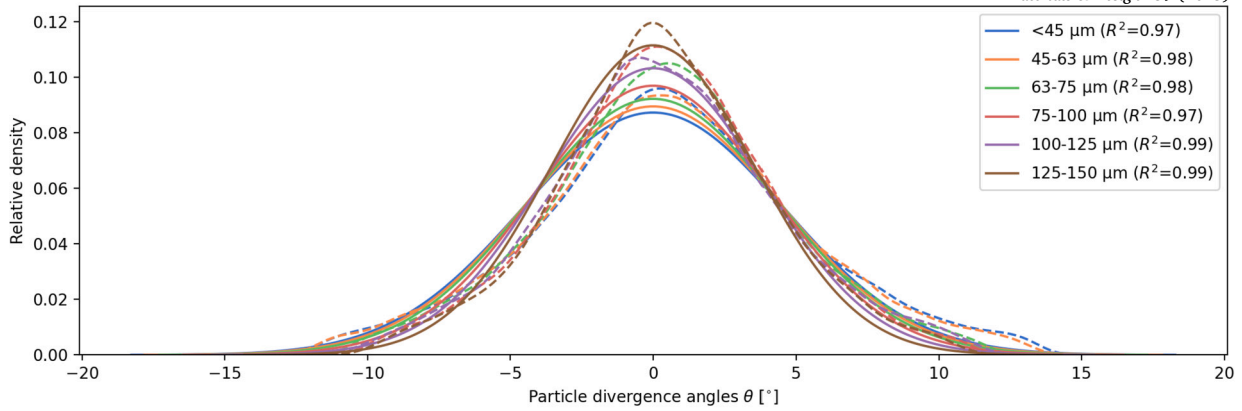


Fig. 14. The modelled particle divergence angle distributions (in solid lines) and KDEs of measured particle divergence angle distributions (in dashed lines) for individual powder particle size fractions. Values of coefficients of determination R^2 measuring the quality of the fit between the modelled and measured divergence angle distribution for each particle size fraction are also displayed.

oriented perpendicularly to the first one, that enabled reconstruction of 3D particle trajectories and calculation of out-of-plane velocity contribution to the 3D particle velocity magnitude as described in Appendix C. As depicted in Fig. 20, the ratio of out-of-plane particle speed to in-plane particle speed remains below 0.1 for all the particle size fractions. The contribution of the particle out-of-plane speed to the three-dimensional velocity magnitude is thus below 0.5%. While a two-camera setup provides this marginal improvement in the accuracy of recovered particle 3D trajectories, it also introduces uncertainties. These stem from particles moving into or out of the focal plane and from larger confidence intervals, as the necessary coupling limits the number of trajectories that can be recovered. The single-camera experimental setup was thus judged more accurate.

It is shown in section Results & analysis that the dependence of mean powder particle speed \bar{v} and standard deviation of powder particle speed σ_v on particle size can be relatively accurately modelled with exponential functions. In the case of divergence angles, linear functions were shown to suffice to describe the relatively weak dependence of mean values $\bar{\theta}$ and standard deviations σ_θ of particle divergence angles on the particle size. Gaussian distributions of particle speeds and divergence angles were shown to produce an excellent fit with the measured distributions when applying the fitted models for \bar{v} , σ_v , $\bar{\theta}$ and σ_θ .

Moreover, the observed trend in mean powder particle speed with the particle size (Fig. 8) appears to fit with the hypothesis that larger particles exit DED nozzle at lower average speeds compared to smaller particles. The current state-of-the-art publications presume that this trend is produced by larger particles with sufficiently high inertia losing energy through plastic rebounds and friction during collisions with the nozzle inner walls, while the smaller particles with lower Stokes numbers follow the carrier gas streamlines and at least partly avoid the loss of energy through collisions with the nozzle walls [13,18,6]. No direct evidence of this mechanism of particle speed segregation was however, detected in the present experimental campaign. The recorded standard deviation of divergence angles in fact exhibits a weak negative correlation with powder particle size (Fig. 13). It is possible that this trend is, at least in part, driven by the particle size relative to the roughness of the nozzle's inner surface. Kovalev et al. [25] observed a decrease in particle divergence angles with decreasing wall roughness. Increasing particle size at constant wall roughness should, at least theoretically, produce a similar effect.

While the relative trends in particle speeds appear to fit with what might be expected from the hypothesized mechanisms of powder-fluid-wall interaction, the absolute values of the powder particle speeds reveal a notable discrepancy. Reader will note that the mean particle speeds for the smaller powder particles (Fig. 8) are considerably higher than the mean carrier gas speed, which can, considering the volumetric flow rate

$Q_g = 5$ L/min of the Argon carrier gas and assuming an incompressible fluid, be estimated at $\bar{u}_g \approx 12$ m/s (for the geometric details of the DED deposition head described in Fig. 4). Reynold's number of the pipe flow within the nozzle channels is below the laminar-transient flow threshold ($Re = 1413 < 2300$), meaning that Poiseuille flow can be assumed. The parabolic fluid velocity profile of Poiseuille flow allows the derivation of maximum carrier gas speed as $u_g^{max} = 2\bar{u}_g \approx 24$ m/s, which matches well with the highest measured values of particle speed (Fig. 10).

Powder particles that continuously bounce off inner nozzle walls should be expected to feature the carrier gas mean axial speed as they effectively continuously traverse the entire channel velocity profile. The fact that the smaller particles used in this study move at a considerably higher axial speed (Appendix D) than the mean carrier gas speed appears to indicate that these particles were concentrating in the central nozzle area with higher mean carrier gas speed. An analysis of the powder particle passages through the nozzle outlet indeed supports this claim as consistently narrower distributions of powder particle locations are observed with diminishing particle size (Appendix E, Fig. 23), but suggests particles must have been in advection-dominated (rather than wall collision-dominated) regime. The particle Stokes numbers vary between $St \approx 6000$ for the smallest particles and $St \approx 20000$ for the largest particles, putting the studied powder particles firmly in the inertia-dominated regime. However, using the approach of Sommerfeld [26], the critical particle diameter d_{cr} , beyond which a two-phase flow is dominated by wall collisions can be determined by calculating the diameter beyond which particle relaxation path is longer than the channel diameter. The critical particle diameter, as proposed by Sommerfeld, depends on the particle's transverse velocity, the distribution of which is known in our case for each powder size fraction. In Appendix F, the distributions of d_{cr} are analysed for all powder fractions and their corresponding distributions of transversal particle speeds. It is shown that while the mean critical diameter for each size fraction is well below the actual particle sizes (suggesting that the particle dynamics is dominated by wall collisions), a smaller portion of the particles up to the size of $d \approx 70 \mu m$ moves at a low enough transverse speed to feature a relaxation path which is shorter than the nozzle inner diameter (Fig. 24). This fits well with the observed data, where particles from the three smallest powder size fractions appear to exceed the mean carrier gas velocity. These results suggest that portions of grains from the three smallest powder size fractions should be in advection-dominated regime and could concentrate in the high velocity region of the nozzle cross-section.

In summary this analysis suggests that speed variation with the powder particle size in DED powder stream indeed exists and is at least partly driven by grain segregation within the DED nozzle. While this does not necessarily negate the energy losses of plastic collisions of larger particles with the nozzle inner walls as a driving mechanism of this effect, no

direct evidence of it was observed during this experimental campaign. It should however be noted that the observed relation between powder particle size and speed has been demonstrated at the given set of carrier gas volumetric flow rate and powder mass flow rate values. While nothing in the present study suggests otherwise, the validity of these findings across the entire spectrum of DED processing parameters is yet to be confirmed.

5. Conclusions

The experimental campaign performed in this study is aimed at analysing the effect of particle size on the particle velocity distribution at the DED nozzle outlet. A novel experimental approach was utilised and powder was separated into different size fractions prior to the high-speed camera experimental runs which allowed us to measure separate velocity distributions for individual powder size fractions. The measured powder velocity distributions were analysed in relationship to the carrier gas velocity to offer a deeper insight into the particle-laden flow in DED processes beyond the narrow scope of the utilized machine. In order to render these results useful for further analysis and facilitate direct comparisons with other measurements, a meticulous analysis of the utilized powder and a thorough description of the experimental setup and post-processing are included in the paper. The main conclusions of this paper can be summarized as follows:

1. Separating the powder into size fractions prior to running the experiments produced excellent results that allowed us to isolate the effect of grain size on powder velocity.
2. A strong negative correlation between the powder particle size and its speed at the DED nozzle outlet was observed.
3. Smaller powder particle fractions were observed to move at average axial speeds exceeding the mean speed of the carrier gas by concentrating in the central high-velocity area of the nozzle cross-section.
4. Spatial grain separation within the nozzle is suggested as an alternative mechanism driving size-dependent particle speed differences.

CRedit authorship contribution statement

Tijan Mede: Writing – original draft, Software, Methodology, Investigation, Funding acquisition, Formal analysis, Conceptualization. **Andrej Jeromen:** Writing – original draft, Methodology, Investigation. **Edvard Govekar:** Writing – review & editing, Supervision. **Michael Mallon:** Writing – review & editing, Supervision. **Matjaž Godec:** Supervision.

Declaration of competing interest

The authors declare that they have no known competing financial interests or personal relationships that could have appeared to influence the work reported in this paper.

Acknowledgements

The authors acknowledge the financial support from The Slovenian Research and Innovation Agency (project No. Z2-4446, research core funding No. P2-0132 and research core funding No. P2-0241).

The investigation was conducted in the scope of the European Space Agency RPA project under Contract No. 4000142691/23/NL/MH/mp.

We would like to thank Gašper Krek for his valuable help during the powder preparation phase.

Appendix A. Deposition head details

Additional dimensional details of the Fraunhofer COAX 12V5 DED deposition head are provided in Fig. 15.

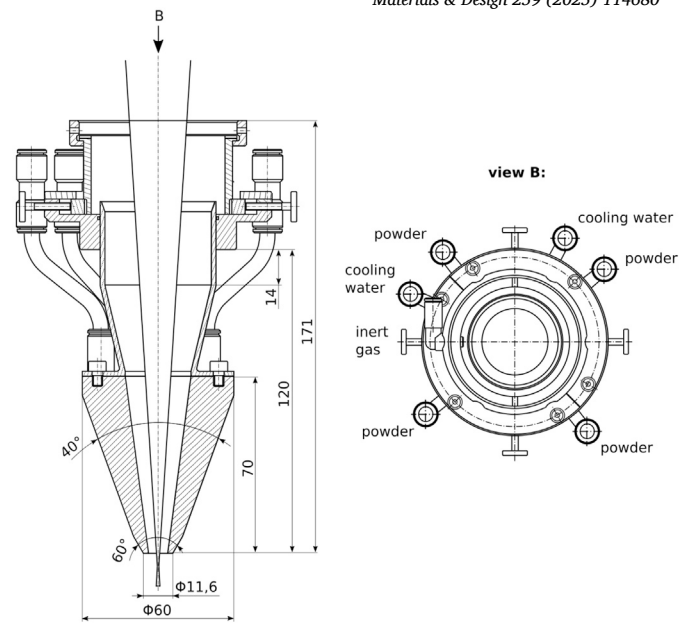


Fig. 15. Dimensional details of the Fraunhofer COAX 12V5 deposition head.

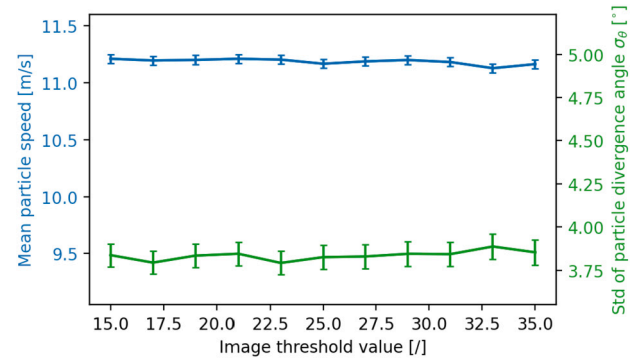


Fig. 16. Sensitivity analysis of measured mean particle speed \bar{v} and standard deviation of divergence angle σ_θ to the image intensity threshold with 95% confidence intervals.

Appendix B. Sensitivity analysis

A sensitivity analysis of the key measured variables to the parameters of image processing was performed in order to set the image processing parameters to correct values and ensure no additional artefacts are introduced to the results by the image processing. The sensitivity analysis was performed on the 75–100 μm powder fraction with base values of image processing parameters: $y_{\text{max}} = 2$ mm, image thresholding value = 25 and clustering distance threshold value = 300.

The influence of image thresholding value (see section Post-processing) on measured mean particle speed \bar{v} and standard deviation of divergence angle σ_θ is analysed in Fig. 16. It can be observed that varying the image thresholding value within a reasonable interval around the grayscale value 25 (which was the utilised value for thresholding) produces only minor fluctuations of the measured variables.

Hierarchical clustering of line candidates for each particle trace (see section Post-processing) forms flat clusters so that the original observations in each flat cluster have no greater a cophenetic distance than clustering distance threshold value. The clustering was performed in the parametric space consisting of coordinates of the two limiting points of each line candidate. The influence of the clustering distance threshold value on measured mean particle speed \bar{v} and standard deviation of divergence angle σ_θ is analysed in Fig. 17. It can be observed that varying the distance threshold value within a reasonable interval around value

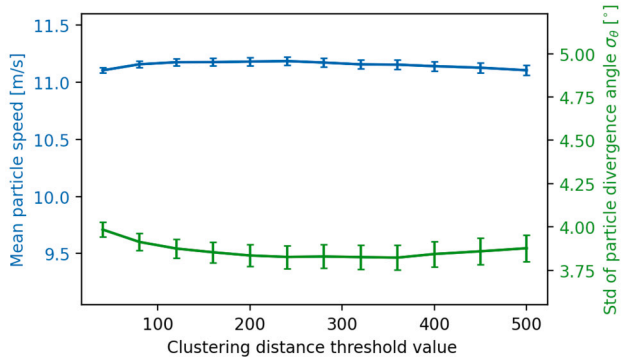


Fig. 17. Sensitivity analysis of measured mean particle speed \bar{v} and standard deviation of divergence angle σ_θ to the clustering distance threshold with 95% confidence intervals.

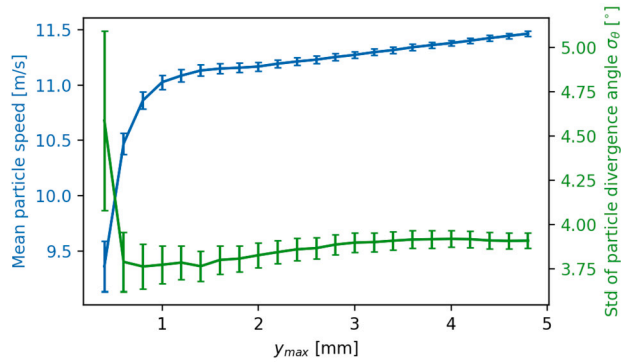


Fig. 18. Sensitivity analysis of measured mean particle speed \bar{v} and standard deviation of divergence angle σ_θ to the vertical threshold of filtered particle traces y_{max} with 95% confidence intervals.

300 (which was the utilised clustering distance threshold value) produces only minor fluctuations of the measured variables.

The influence of the vertical threshold distance of filtered particle traces from the nozzle y_{max} (see Fig. 6) on measured mean particle speed \bar{v} and standard deviation of divergence angle σ_θ is analysed in Fig. 18. It can be observed that the interval $y_{max} < 1$ mm is marked by strong fluctuations and large confidence intervals of both measured variables. In the range $1 \text{ mm} < y_{max} < 2$ mm, the fluctuations of the measured values stabilize and the confidence intervals diminish due to a significant increase in the available sample size. The vertical threshold distance of filtered particle traces from the nozzle $y_{max} = 2$ mm is hence chosen as appropriate.

Appendix C. Particle out-of-plane velocities

A secondary camera was also utilized in the experimental setup described in section 2.2, which allowed us to estimate the measurement error due to out-of-plane velocity of powder particles. The secondary camera was placed at the same distance as the primary camera, but it was oriented perpendicularly to the first one (and parallel to the laser light plane) as depicted in Fig. 19. During the execution of the experiment, the two cameras were triggered to capture images in unison, which allowed the use of these pairs of images to reconstruct 3D trajectories of the passing powder particles. Initial calibration was performed to assure image scales and offsets were aligned. Identification of particle traces and evaluation of particle speed was performed in each image separately as described in section 2.3. Identified particle traces from both images were then paired by finding trace pairs with matching vertical coordinates of the starting and ending points. Certain discrepancy was allowed in matching the vertical coordinates in order to account for the

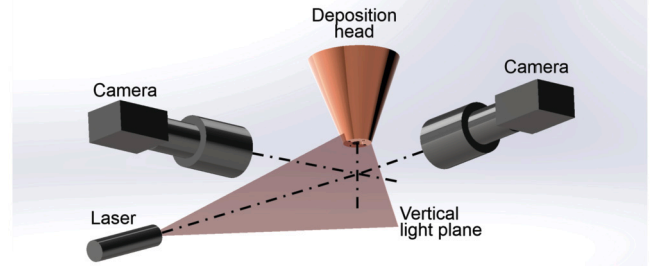


Fig. 19. Schematic representation of the experimental setup.

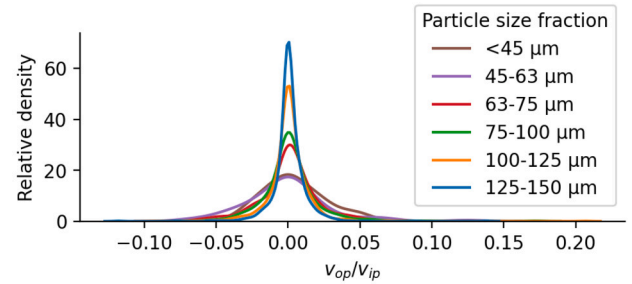


Fig. 20. Distributions of the ratio of the out-of-plane particle speed v_{op} to in-plane particle speed v_{ip} for individual powder particle size fractions.

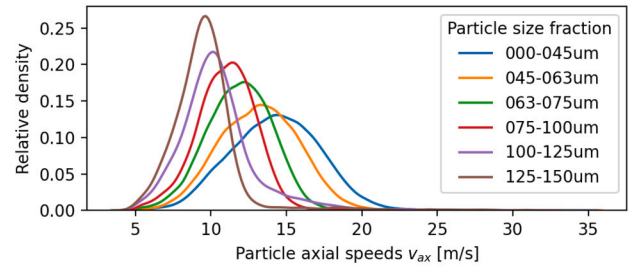


Fig. 21. KDEs of measured particle axial speed v_{ax} distributions for individual powder particle size fractions.

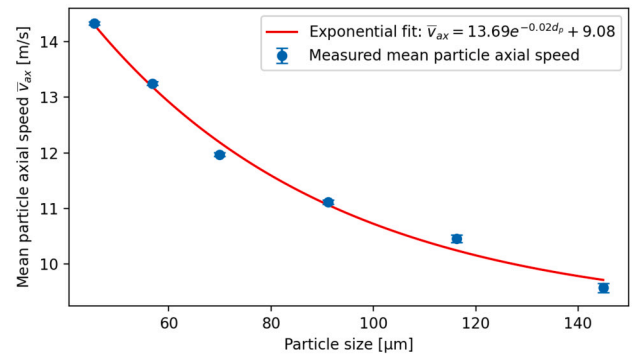


Fig. 22. Measured mean values of particle axial speed \bar{v}_{ax} as a function of particle size d_p with 95% confidence intervals (in blue) and a fitted exponential function (in red).

imperfections in the camera calibration, non-homogeneous reflection of light and artefacts of the trace recognition algorithm.

Fig. 20 represents the measured distributions of the ratios of particle out-of-plane speed to particle in-plane speed v_{op}/v_{ip} for each powder size fraction respectively. In-plane speed refers to the magnitude of particle velocity perpendicular to the axis of the primary camera and out-of-plane speed refers to the magnitude of particle velocity parallel with the axis of the primary camera. The distributions of v_{op}/v_{ip} are

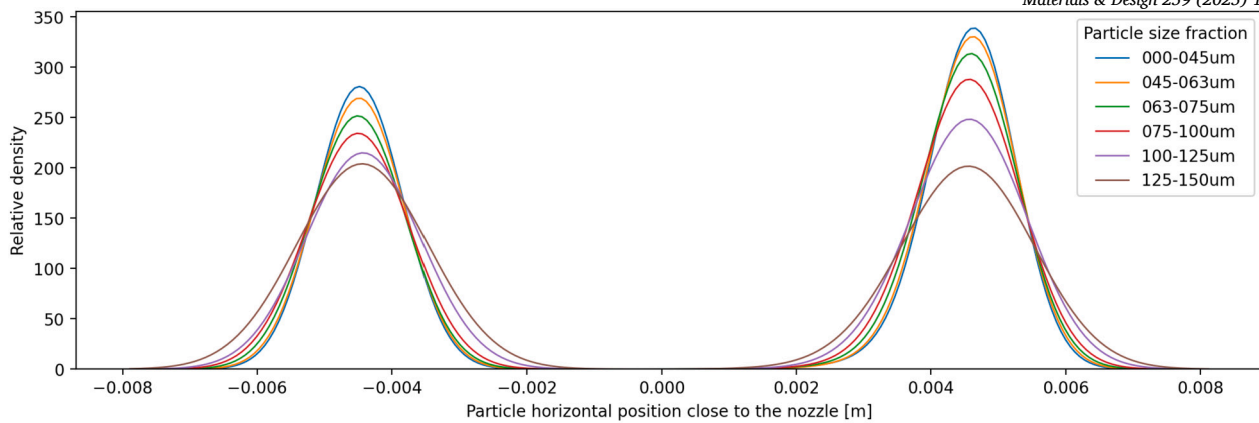


Fig. 23. Distributions of measured x-coordinates of particle positions at the nozzle outlet for each powder particle size fraction.

largely contained within the $[-0.05, 0.05]$ interval, with the smaller particle size fractions extending into the $[-0.1, 0.1]$ interval. At ratio $v_{op}/v_{ip} = 0.1$, the contribution of the particle out-of-plane speed to the three-dimensional velocity magnitude is roughly 5%.

Appendix D. Particle axial speeds

Particle axial speeds v_{ax} at the DED nozzle outlet are analysed in this appendix, where axial speed refers to the component of particle velocity parallel to the nozzle axis (Fig. 4). Fig. 21 represents the KDEs of particle axial speed distributions for individual powder size fractions. Very similar distributions to those in Fig. 7 can be observed with somewhat diminished absolute speed values. Fig. 22 depicts the mean axial particle speeds as function of the powder particle size. Again, a very similar trend to that observed in Fig. 8 can be observed with marginally diminished absolute values of speed.

Appendix E. Particle positions at the nozzle outlet

Particle positions close to the nozzle outlets were analysed to provide additional evidence of particle segregation inside the nozzle. This was achieved by filtering out the particle traces with the vertical coordinate (y_c) of the central point of the trace within $y_{max} = 2$ mm of the nozzle outlet (Fig. 6). Trajectories of these particle traces were extrapolated to the nozzle outlet, where the horizontal (x) coordinate of the trajectory was recorded. The procedure was repeated for all of the powder particle size fractions and KDEs of the resulting distributions are plotted in Fig. 23. Distributions of particle horizontal positions at nozzle outlets exhibit two distinct sets of peaks - one for each of the two observed nozzles. An increasing dispersion of the curves is consistently observed with increasing particle size. This supports the claim of smaller particle exhibiting higher concentrations in the central area of the nozzle cross section.

Appendix F. Critical particle diameters

Using the approach of Sommerfeld [26], the critical particle diameter d_{cr} , beyond which a two-phase flow is dominated by wall collisions can be determined by calculating the diameter beyond which particle relaxation path is longer than the channel diameter. Sommerfeld proposed to estimate the transversal speeds as a fraction of axial speeds. This is however not needed in this analysis, as the transversal speeds of individual particle traces are known. Since Sommerfeld's critical particle diameter depends on the transversal speed and since each particle fraction exhibits a different spectrum of transversal speeds, the critical particle diameter is presented as a distribution of values (corresponding to the distribution of transversal speeds) for each particle size fraction as shown in Fig. 24. While the mean critical diameter for each size fraction

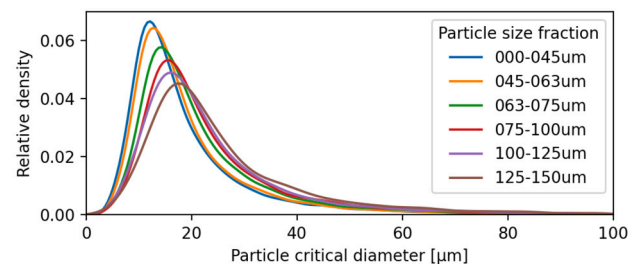


Fig. 24. Distributions of critical particle diameters [26] for each powder particle size fraction and corresponding to the actual distribution of transversal speeds in that powder fraction.

is well below the actual particle sizes, the smaller powder particle fractions exhibit a part of the critical diameter distributions that is beyond the actual particle sizes. This means that a fraction of the powder particles moved with a sufficiently low transverse speed for their relaxation path to be shorter than the inner diameter of the nozzle.

Appendix G. Supplementary material

Supplementary data associated with this article can be found in an online repository at <https://osf.io/s5nkj/> with identifier DOI <https://doi.org/10.17605/OSF.IO/S5NKJ>. Due to repository size considerations, only a subset of captured images was uploaded for each experimental run.

Data availability

A 'Data Availability' statement is included in the paper.

References

- [1] J.H. Martin, B.D. Yahata, J.M. Hundley, J.A. Mayer, T.A. Schaedler, T.M. Pollock, 3d printing of high-strength aluminium alloys, *Nature* 549 (7672) (2017) 365–369.
- [2] C. Thompson, Additive manufacturing for tool manufacturing and repair in reduced gravity environments-a survey, 2024.
- [3] T.D. Ngo, A. Kashani, G. Imbalzano, K.T. Nguyen, D. Hui, Additive manufacturing (3d printing): a review of materials, methods, applications and challenges, *Composites, Part B, Eng.* 143 (2018) 172–196.
- [4] M. Hoffmann, A. Elwany, In-space additive manufacturing: a review, *J. Manuf. Sci. Eng.* 145 (2) (2023) 020801.
- [5] S. Wen, Y. Shin, J. Murthy, P. Sojka, Modeling of coaxial powder flow for the laser direct deposition process, *Int. J. Heat Mass Transf.* 52 (25–26) (2009) 5867–5877.
- [6] O. Kovalev, I. Kovaleva, I.Y. Smurov, Numerical investigation of gas-disperse jet flows created by coaxial nozzles during the laser direct material deposition, *J. Mater. Process. Technol.* 249 (2017) 118–127.
- [7] Z. Liu, H.-C. Zhang, S. Peng, H. Kim, D. Du, W. Cong, Analytical modeling and experimental validation of powder stream distribution during direct energy deposition, *Addit. Manuf.* 30 (2019) 100848.

- [8] S.M. Thompson, L. Bian, N. Shamsaei, A. Yadollahi, An overview of direct laser deposition for additive manufacturing; part I: transport phenomena, modeling and diagnostics, *Addit. Manuf.* 8 (2015) 36–62.
- [9] Y.-L. Huang, J. Liu, N.-H. Ma, J.-G. Li, Three-dimensional analytical model on laser-powder interaction during laser cladding, *J. Laser Appl.* 18 (1) (2006) 42–46.
- [10] J. Wu, P. Zhao, H. Wei, Q. Lin, Y. Zhang, Development of powder distribution model of discontinuous coaxial powder stream in laser direct metal deposition, *Powder Technol.* 340 (2018) 449–458.
- [11] J. Lin, Numerical simulation of the focused powder streams in coaxial laser cladding, *J. Mater. Process. Technol.* 105 (1–2) (2000) 17–23.
- [12] S. Zekovic, R. Dwivedi, R. Kovacevic, Numerical simulation and experimental investigation of gas–powder flow from radially symmetrical nozzles in laser-based direct metal deposition, *Int. J. Mach. Tools Manuf.* 47 (1) (2007) 112–123.
- [13] P. Balu, P. Leggett, R. Kovacevic, Parametric study on a coaxial multi-material powder flow in laser-based powder deposition process, *J. Mater. Process. Technol.* 212 (7) (2012) 1598–1610.
- [14] H. Tan, C. Zhang, W. Fan, F. Zhang, X. Lin, J. Chen, W. Huang, Dynamic evolution of powder stream convergence with powder feeding durations in direct energy deposition, *Int. J. Mach. Tools Manuf.* 157 (2020) 103606.
- [15] O.d.O.D. Neto, R.M.C. d, S. Vilar, Interaction Between the Laser Beam and the Powder Jet in Blown Powder Laser Alloying and Cladding, *International Congress on Applications of Lasers & Electro-Optics*, vol. 1998, Laser Institute of America, 1998, pp. D180–D188.
- [16] O. Diniz Neto, R. Vilar, Physical–computational model to describe the interaction between a laser beam and a powder jet in laser surface processing, *J. Laser Appl.* 14 (1) (2002) 46–51.
- [17] Y. Fu, A. Lored, B. Martin, A. Vannes, A theoretical model for laser and powder particles interaction during laser cladding, *J. Mater. Process. Technol.* 128 (1–3) (2002) 106–112.
- [18] S. Liu, Y. Zhang, R. Kovacevic, Numerical simulation and experimental study of powder flow distribution in high power direct diode laser cladding process, *Lasers Manuf. Mater. Proc.* 2 (2015) 199–218.
- [19] Q. Chai, X. He, Y. Xing, G. Sun, Numerical study on the collision effect of particles in the gas-powder flow by coaxial nozzles for laser cladding, *Opt. Laser Technol.* 163 (2023) 109449.
- [20] Y. Huang, M.B. Khamesee, E. Toyserkani, A comprehensive analytical model for laser powder-fed additive manufacturing, *Addit. Manuf.* 12 (2016) 90–99.
- [21] O. Kovalev, A. Zaitsev, D. Novichenko, I. Smurov, Theoretical and experimental investigation of gas flows, powder transport and heating in coaxial laser direct metal deposition (dmd) process, *J. Therm. Spray Technol.* 20 (2011) 465–478.
- [22] I. Smurov, M. Doubenskaia, S. Grigoriev, A. Nazarov, Optical monitoring in laser cladding of ti6al4v, *J. Therm. Spray Technol.* 21 (2012) 1357–1362.
- [23] C. Katinas, W. Shang, Y.C. Shin, J. Chen, Modeling particle spray and capture efficiency for direct laser deposition using a four nozzle powder injection system, *J. Manuf. Sci. Eng.* 140 (4) (2018).
- [24] A. Jeromen, A. Vidergar, M. Fujishima, G.N. Levy, E. Govekar, Powder particle–wall collision-based design of the discrete axial nozzle-exit shape in direct laser deposition, *J. Mater. Process. Technol.* 308 (2022) 117704.
- [25] O. Kovalev, D. Bedenko, A. Gurin, D. Sergachev, Study of optimization features of gas-powder jets created by a coaxial nozzle with divided powder supply during direct laser deposition of materials, *Opt. Laser Technol.* 181 (2025) 112020.
- [26] M. Sommerfeld, Modelling of particle-wall collisions in confined gas-particle flows, *Int. J. Multiph. Flow* 18 (6) (1992) 905–926.